Computers and Geotechnics 155 (2023) 105224

Contents lists available at ScienceDirect

Computers and Geotechnics

journal homepage: www.elsevier.com/locate/compgeo

# Modelling hydro-mechanical coupled behaviour of unsaturated soil with two-phase two-point material point method

Z.Q. Zhan [a], C. Zhou [a,*], C.Q. Liu [b,*], C.W.W. Ng [c]

[a] Department of Civil and Environmental Engineering, The Hong Kong Polytechnic University, Hung Hom, Kowloon, Hong Kong
[b] State Key Laboratory of Nonlinear Mechanics, Institute of Mechanics, Chinese Academy of Sciences, Beijing 100090, China
[c] Department of Civil and Environmental Engineering, Hong Kong University of Science and Technology, Clear Water Bay, Kowloon, Hong Kong

ARTICLE INFO

*Keywords:*
Material point method
Unsaturated soil
Hydro-mechanical coupling
Large deformation
Landslide

ABSTRACT

Material point method (MPM) offers an effective approach for analysing large-deformation problems, such as landslides that often involve unsaturated soil. Several MPM formulations for unsaturated soil have been reported in the literature, but they assumed that water retention ability and permeability function are independent of soil deformation. Furthermore, most studies used a single set of material points, so they cannot simulate some processes (e.g., the infiltration of free water into unsaturated soil). To address these problems, a two-point MPM formulation has been extended from saturated to unsaturated soils, considering the influence of porosity change on the water retention curve and permeability function. The information of solid and liquid phases is carried by two individual sets of material points, assuming zero air pressure. The elastoplastic mechanical behaviour is modelled by the Drucker-Prager model using Bishop's stress. The MPM simulations were compared with the results of physical model tests (for large-deformation problems) and finite element analysis (for small-deformation problems). It is evident that the proposed MPM formulation is able to capture various hydro-mechanical problems well. In particular, the computed failure processes of unsaturated soil slope under rainfall are consistent with results from physical model tests.

## 1. Introduction

Many geotechnical problems involve large deformations, such as the post-failure dynamics of landslides and pile driving (Lv et al., 2014; Song et al., 2018). They cannot be easily reproduced using the finite element method (FEM) because of the mesh distortion. Several numerical methods have been proposed for large deformation problems, such as the Arbitrary Lagrangian-Eulerian (ALE), Coupled Eulerian-Lagrangian (CEL) approach, Updated Lagrangian Finite Element (ULFE), Smooth Particle Hydrodynamics (SPH), Finite-element method with Lagrangian integration points (FEMLIP), Discrete Element Method (DEM) and Material Point Method (MPM) (Hu and Randolph, 1998; Khoshghalb and Khalili, 2015; Wang et al., 2015; Shafee and Khoshghalb, 2022). The MPM is an improved particle-in-cell (PIC) method, where the Lagrangian (Lagrangian point masses) and Eulerian (Eulerian background mesh) descriptions are both applied (Sulsky et al., 1994). It is an effective method for large-deformation problems involving fluid–solid interactions, such as rainfall-induced failure of unsaturated soil slopes (Soga et al., 2016). Hence, this work focuses on developing MPM formulations, which will be used to study rainfall-induced landslides in further studies.

So far, the MPM has been applied to analyse a number of problems like landslides (Fern et al., 2017; Soga et al., 2016; Yerro et al., 2016a, b), the failure of dikes (Martinelli et al., 2017) and the collapse of retaining walls (Więckowski, 2004; Beuth, 2012). Most previous studies focused on saturated soil, a two-phase material comprising solid particles and liquid waters, with two distinct schemes (i.e. representing saturated soil using one set or two sets of material points).

In the two-phase one-point scheme, a single set of Lagrangian material points are used to carry the information for both solid and liquid phases. Material points are attached to the soil skeleton, and the motion of the liquid phase is described with reference to the motion of the solid phase. By using such a scheme, Zhang et al. (2009) proposed a MPM approach based on the $\boldsymbol{u}^s - p^l$ form governing equations, where $\boldsymbol{u}^s$ is the displacement of the solid phase and $p^l$ is the liquid pressure. Zabala & Alonso (2011) simulated the failure of the Aznalcollar tailings dam with the $\boldsymbol{u}^s - p^l$ formulation and a Mohr-Coulomb elastoplastic model

* Corresponding authors.
*E-mail addresses:* zhiqi.zhan@connect.polyu.hk (Z.Q. Zhan), c.zhou@polyu.edu.hk (C. Zhou), chuanqil@imech.ac.cn (C.Q. Liu), cecwwng@ust.hk (C.W.W. Ng).

https://doi.org/10.1016/j.compgeo.2022.105224
Received 12 August 2022; Received in revised form 1 December 2022; Accepted 24 December 2022
Available online 4 January 2023

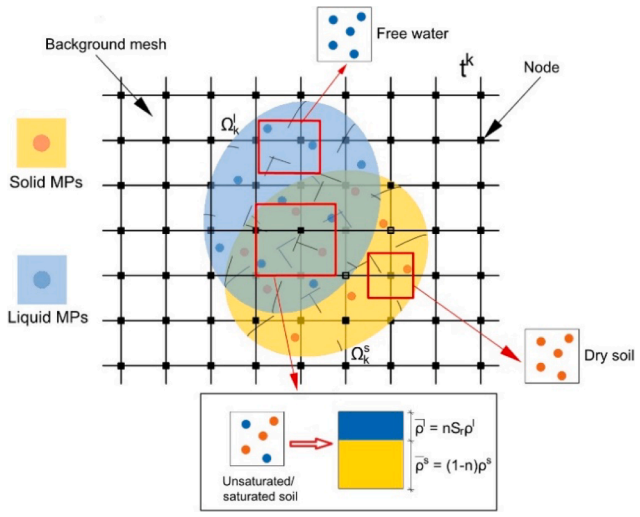


**Fig. 1.** Schematic diagram of the two-phase two-point MPM approach for simulation.

modified with strain-softening. In the $\boldsymbol{u}^s - p^l$ formulation, two mesh size-related step criteria should be satisfied because of the different primary unknowns for the solid and liquid phases (Verruijt, 2009). For a small-size mesh, the second compression wave cannot be captured accurately because the $p^l$-dependendt time step is too short (Van Esch et al., 2011). Thereby, Jassim et al. (2013) developed a two-phase one-point MPM with the $\boldsymbol{u}^s - \boldsymbol{u}^l$ formulation, where $\boldsymbol{u}^l$ is the displacement of the liquid phase.

Representing saturated soil with a single set of material points is computationally efficient, but it has some limitations. For instance, it cannot simulate important problems such as rainfall-induced ponding, internal erosion and liquid-like response mixture. In addition, it is unsuitable for problems with a high relative acceleration between the liquid and solid (Zienkiewicz et al., 1990). To address these problems, some researchers have adopted the two-phase two-point scheme, using two sets of material points for the solid and liquid phases. Abe et al. (2014) used a two-phase two-point MPM to study the failure process of a river levee embankment by using the $\boldsymbol{u}^s - p^l$ formulation. Bandara & Soga (2015) extended the $\boldsymbol{u}^s - \boldsymbol{u}^l$ formulation of Jassim et al. (2013) using the two-phase two-point MPM. Based on the work of Bandara & Soga (2015), Liu et al. (2017) developed a three-dimensional two-phase two-point MPM code, which used the generalised interpolation material point method (GIMP) for spatial discretisation. The GIMP can decrease numerical oscillations compared with the standard MPM during the calculation process.

Recently, the MPM has also been applied to simulate unsaturated soil. Unsaturated soil is a mixture of solid, liquid and gas, and it is relevant to many geotechnical problems like rainfall-induced landslides (Ng et al., 2020; Zhou and Ng, 2016). Similar to the modelling of saturated soil, several schemes have been proposed for unsaturated soil. Higo et al. (2010) proposed an MPM-FDM coupled numerical method for unsaturated soil and the $\boldsymbol{u}^s - p^l$ form governing equations were applied. Yerro et al. (2015) improved the $\boldsymbol{u}^s - \boldsymbol{u}^l$ formulation (Jassim et al., 2013) and developed a three-phase one-point MPM approach. The momentum balance of solid, liquid and gas was adopted to govern their motion. Alternatively, some researchers (e.g. Wang et al., 2018; Lei et al., 2020; Ceccato et al., 2021) neglected the gas density and gas pressure and proposed a simplified approach for modelling unsaturated soil with the two-phase one-point MPM, which uses the $\boldsymbol{u}^s - \boldsymbol{u}^l$ formulation. Feng et al. (2021) proposed a two-phase two-point MPM for saturated and unsaturated soil to simulate the dynamic interaction of free water and soils. It should be pointed out that the influence of porosity change on water retention function and permeability function was not considered in the existing MPM formulations for unsaturated soil.

In this study, a two-phase two-point MPM formulation was developed based on Liu et al. (2017). It is suitable for solving large deformation problems involving saturated and unsaturated soils. The solid and liquid phases are represented by two individual sets of material points, so solid and liquid movements can be simulated, respectively. Gas density and pressure are not considered. The GIMP is adopted for space discretisation to minimise the problem of numerical oscillations. The governing equations, space discretisation, time discretisation, computational procedures and model verifications are introduced in the following sections. Analyses of rainfall-induced landslides are also presented, highlighting the importance of rainfall in unsaturated soil slope failure initiation and propagation.

For the symbol convention, for example, in $\dot{\boldsymbol{a}}_k^{\alpha}$, the superscript $\alpha$ can be $s$ and $l$, representing the solid and water phases, respectively, and the variable without $\alpha$ is for the mixture; $k$ means the time step $k$; the bold $\boldsymbol{a}$ means tensor; the dot is the time derivative. Regarding the sign convention, the tension in the solid phase and compression in the liquid phase are positive.

## 2. Governing equations

Unsaturated soil is a three-phase material comprising solid particles, liquid and gas. A comprehensive model should incorporate governing equations for all phases. However, the modelling can be simplified for most geotechnical problems, where the pore air in unsaturated soil is connected to the atmosphere and its pressure is maintained at zero. With this simplification, a two-phase two-point MPM approach is proposed for analysing the hydro-mechanical problems involving unsaturated soil. The continuum body is divided into a finite number of subdomains represented by two sets of material points, as shown in Fig. 1. They carry the information of the liquid and solid phases, respectively. No material point is required for the gas phase.

To describe the volume fraction of solid and liquid phases, porosity $n$ and degree of saturation $S_r$ are used. The volume fractions for the solid phase and liquid phase are equal to $1-n$ and $nS_r$, respectively. Apart from the subdomains for unsaturated soil, the two-phase two-point MPM approach can simulate several extreme conditions in a unified approach, including (a) saturated soil with $S_r = 1$; (b) dry soil for which the subdomains are occupied by solid material points only and $S_r$ is equal to 0; (c) free water (i.e. water outside soil skeleton) for which there are only liquid material points in the subdomains with $S_r = 1$ and $n = 1$.

In addition, the governing equations are based on the following assumptions: (i) soil particles are incompressible; (ii) the transfer of water vapour is negligible; (iii) the temperature is constant and uniform.

### 2.1. Momentum balance equations

The relative motion of liquid and solid phases can be considered in the two-phase two-point MPM. Two momentum balance equations are used to calculate the acceleration of liquid and solid phases.

For the liquid phase, the momentum balance is as follows:

$$\rho^l \dot{\boldsymbol{v}}^l = \boldsymbol{F}_d^l - \nabla p^l + \rho^l \boldsymbol{g} \tag{1}$$

where $\rho^l$ is the density of the liquid phase, $\dot{\boldsymbol{v}}^l$ is the acceleration of the liquid phase, $\boldsymbol{g}$ is the gravitational acceleration, and $\boldsymbol{F}_d^l$ is the drag force imposed by the solid–fluid interaction. The drag force is governed by Darcy's law when a laminar and steady flow in a low-velocity regime is simulated:

$$\boldsymbol{F}_d^l = -\frac{nS_r\rho^l g}{k}\left(\boldsymbol{v}^l - \boldsymbol{v}^s\right) \tag{2}$$

where $\boldsymbol{v}^l$ is the velocity of the liquid phase, $\boldsymbol{v}^s$ is the velocity of the solid phase, $k$ is the permeability. It should be pointed out that in the nu-

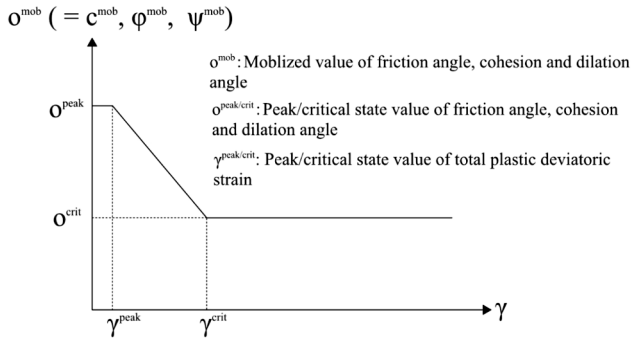


**Fig. 2.** Mobilisation of friction angle, dilation angle and cohesion with plastic shear strain (after Bandara & Soga, 2015).

merical simulations carried out in this study, the water flow velocity and Reynolds number are relatively small. Darcy's law is applied for simplicity with the assumption of laminar flow. The relationship between drag force and relative velocity is thus linear, as shown in Eq. (2). A nonlinear formulation should be considered if turbulent water flow is involved (e.g., wave-overtopping and post-failure motion of soil slope). A detailed description of this modification in MPM analysis was reported by Ceccato et al. (2018).

For the case of free water, the drag force is zero, and Eq. (1) reduces to the following equation:

$$\rho^l \dot{\boldsymbol{v}}^l = -\nabla p^l + \rho^l \boldsymbol{g} \tag{3}$$

The solid–fluid mixture needs to meet both linear and angular momentum balances. Since the tensor of total stress $\boldsymbol{\sigma}$ is symmetric, the angular momentum is always fulfilled. The linear momentum balance is described by

$$(1-n)\rho^s \dot{\boldsymbol{v}}^s + nS_r\rho^l \dot{\boldsymbol{v}}^l = div(\boldsymbol{\sigma}) + (1-n)\rho^s \boldsymbol{g} + nS_r\rho^l \mathrm{g} \tag{4}$$

where $\rho^s$ is the density of the solid phase (i.e. soil particles), $\dot{\boldsymbol{v}}^s$ is the acceleration of the solid phase.

From the above momentum balance equations for the liquid and solid–fluid mixture, the acceleration of liquid and solid phases can be obtained.

### 2.2. Mass balance equations

The mass balance of the solid phase is given by

$$\frac{\partial}{\partial t}[\rho^s(1-n)] + div[\rho^s(1-n)\boldsymbol{v}^s] = 0 \tag{5}$$

By assuming that soil particles are incompressible ($\frac{\partial \rho^s}{\partial t} \approx 0$ and $\nabla \rho^s \approx 0$), Eq. (5) is reduced to Eq. (6):

$$\frac{\partial n}{\partial t} = (1-n)div(\boldsymbol{v}^s) - \boldsymbol{v}^s \nabla n \tag{6}$$

Similarly, the mass balance of the liquid phase is given by the following equation:

$$\frac{\partial}{\partial t}(nS_r\rho^l) + div(nS_r\rho^l \boldsymbol{v}^l) = 0 \tag{7}$$

Since water is only weakly compressible, the gradient of the water density is negligible ($\nabla \rho^l \approx 0$). In addition, $\frac{1}{\rho^l}\frac{\partial \rho^l}{\partial p^l} = \frac{1}{K^l}$, where $K^l$ is the compressibility of the liquid phase. The following equation can be therefore derived based on Eq. (7):

$$n\left(\frac{S_r}{K^l} + \frac{\partial S_r}{\partial p^l}\right)\frac{\partial p^l}{\partial t} + S_r\frac{\partial n}{\partial t} + nS_r div(\boldsymbol{v}^l) + \boldsymbol{v}^l \nabla\left(nS_r\right) = 0 \tag{8}$$

Substituting Eq. (6) into Eq. (8), it is obtained that:

$$n\left(\frac{S_r}{K^l} + \frac{\partial S_r}{\partial p^l}\right)\frac{\partial p^l}{\partial t} = -S_r\left[(1-n)div(\boldsymbol{v}^s) - \boldsymbol{v}^S\nabla n + ndiv(\boldsymbol{v}^l) + \boldsymbol{v}^l\frac{\nabla(nS_r)}{S_r}\right] \tag{9}$$

Eq. (9) can update the pore water pressure under both saturated and unsaturated conditions. Furthermore, for the condition of free water with $S_r = 1$ and $n = 1$, Eq. (9) reduces to the following equation:

$$\frac{\partial p^l}{\partial t} = -K^l div(\boldsymbol{v}^l) \tag{10}$$

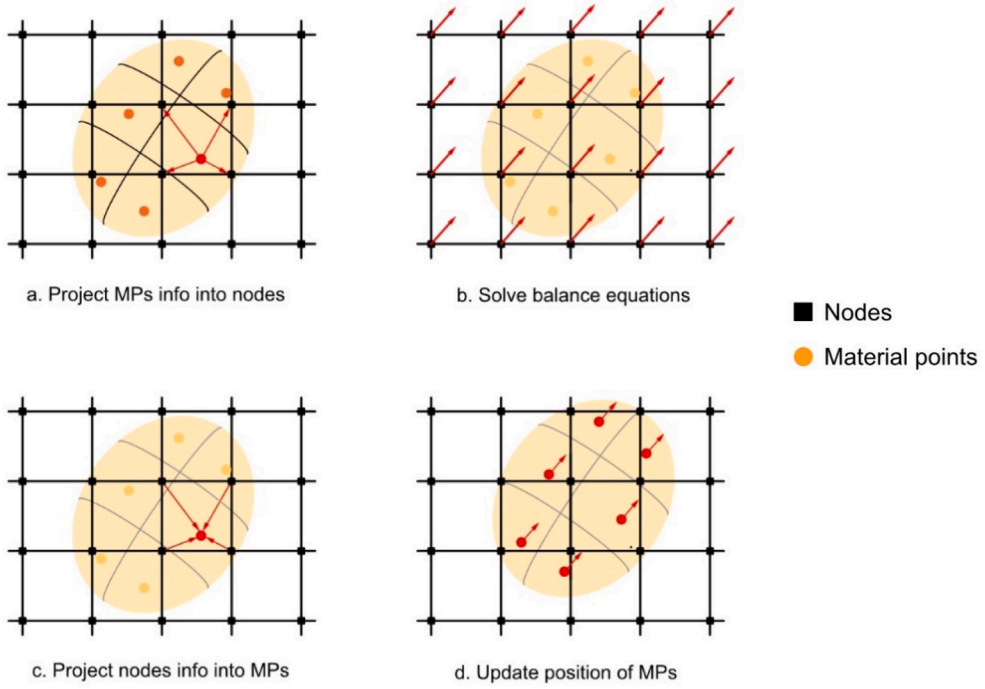


**Fig. 3.** Computation procedures of MPM (after Fern, 2016).

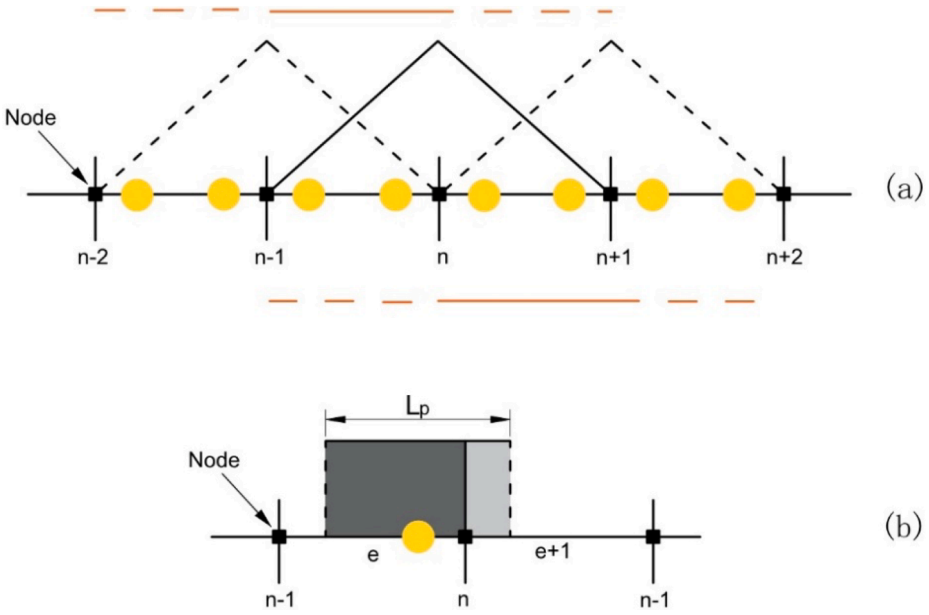


**Fig. 4.** (a) Linear shape functions (black line) and piecewise constant gradients of linear shape functions for standard MPM (orange line); (b) characteristic function and treating the grid crossing problem in GIMP (after Fern et al., 2019). (For interpretation of the references to colour in this figure legend, the reader is referred to the web version of this article.)

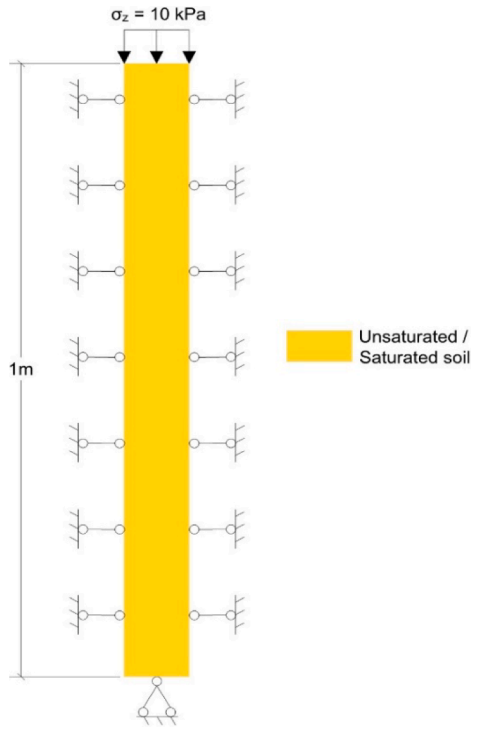


**Fig. 5.** Simulation of 1D consolidation of a soil column: geometry and boundary conditions.

### 2.3. Constitutive equations for the mechanical behaviour

Many stress state variables have been proposed for unsaturated soil in the literature. The Bishop's stress is applied in this study:

$$\boldsymbol{\sigma}^* = \boldsymbol{\sigma} + \chi p^l \boldsymbol{\delta} \tag{11}$$

where $\boldsymbol{\sigma}^*$ is the Bishop's stress tensor, $\chi$ is the Bishop parameter, and it is simplified as $S_r$, $\boldsymbol{\delta}$ is the delta function. As discussed above, the saturated condition can be considered an extreme case of unsaturated condition with a degree of saturation of 100 % (Ng et al., 2020). In this extreme condition, the Bishop's stress reduces to Terzaghi's effective stress. Thus, the use of Bishop's stress can ensure a smooth transition between saturated and unsaturated conditions.

**Table 1**
Material characteristics for 1D consolidation and free water infiltration test.

| | |
|---|---|
| Water bulk modulus, $K^l$ | 2.2 GPa |
| Solid density, $\rho^s$ | 2600 kg/m$^3$ |
| Water density, $\rho^l$ | 1000 kg/m$^3$ |
| Solid Young's modulus, E | 10 MPa |
| Poisson's ratio, $\nu$ | 0.33 |
| Porosity, n | 0.4 |
| Saturated permeability, $k_{sat}$ | $9.8 \times 10^{-4}$ m/s |
| $S_{res}$ | 0 |
| a | 12 |
| $\lambda$ | 0.09 |

Using Bishop's stress, the Drucker–Prager model with strain hardening/softening is used to model the behaviour of saturated and unsaturated soils. Depending on its state, soil shows strain hardening or softening behaviour (Chiu & Ng, 2003; Ng et al., 2020). In the current study, the strain hardening/softening is modelled using the simplified approach of Bandara & Soga (2015). The key idea is shown in Fig. 2. The mobilised cohesion $c$, dilation angle $\psi$ and friction angle $\varphi$ are all functions of the total plastic shear strain after the onset of plastic yielding. Details of this method were reported by Bandara & Soga (2015).

Apart from the stress state variables and the incorporation of strain hardening/softening, all other mathematical formulations from the Drucker–Prager model can be equally applied here. Since details of the Drucker–Prager model are widely reported in the literature, they are not repeated here.

In this study, the objective Jaumman stress rate is employed to alleviate the rotation influence on the stress measure, as illustrated in Liu et al. (2017). As a discussion, the MPM is a kind of updated Lagrangian description in the finite-strain framework. A work-conjugate pair of strain and stress is necessary for a completed formulation.

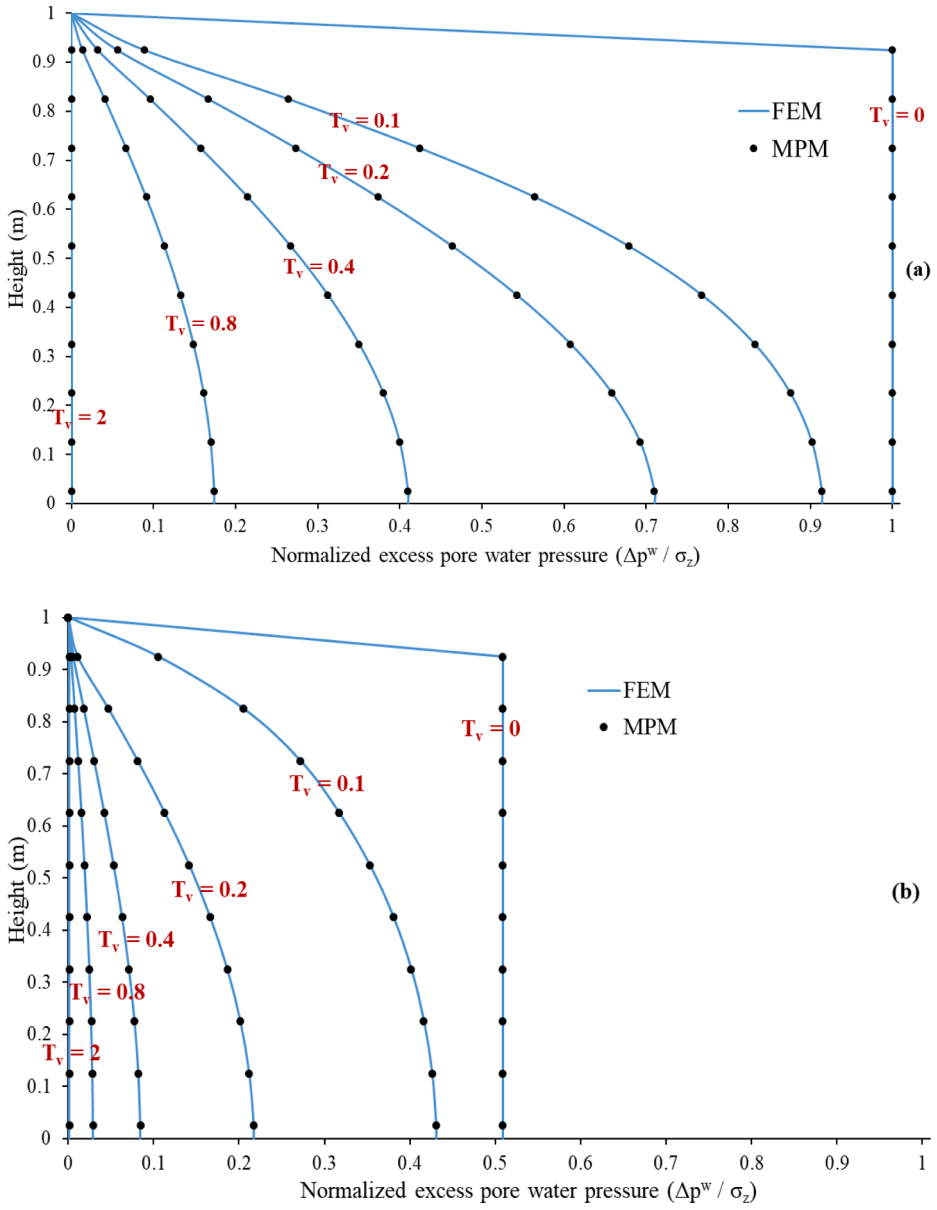


**Fig. 6.** Comparisons between FEM and MPM results of 1D consolidation tests: (a) saturated condition and (b) unsaturated condition.

Although the object Jaumann stress rate is adopted in this work, the strain measure is not specially treated rather than the symmetry part of the gradient of the displacements for simplicity, which is also employed in Zhang et al. (2016) and Fern et al. (2019). The results look good though a mathematically completed formulation is not exactly followed, probably attributed to the meshless method with resetting the background grid at the beginning of each time step. Recently, there have been some works (Liu & Sun, 2020; de Vaucorbeil et al., 2020) developing the MPM approach within the finite-strain framework to avoid the drawbacks of the formulation mentioned above.

### 2.4. Constitutive equations for the hydraulic behaviour

Soil water retention curve (SWRC) is important in modelling unsaturated soil behaviour (Zhou et al., 2020). The current study adopts the SWRC model of Tarantino (2009), developed from van Genuchten's (1980) model by incorporating the influence of porosity. The relationship between the effective degree of saturation ($S_{eff}$) and pore water pressure is described as follows:

$$S_{eff} = \frac{S_r - S_{res}}{1 - S_{res}} = \left[1 + \left(a\frac{se^b}{\rho^l g}\right)^{\frac{1}{1-\lambda}}\right]^{-\lambda} \tag{12}$$

where

$$e = \frac{n}{1-n} \tag{13a}$$

$$b = \frac{1-\lambda}{\lambda} \tag{13b}$$

where $S_{res}$ is the residual degree of saturation, $s$ is the matric suction, $a$ and $\lambda$ are model parameters related to the pore size distribution of soil, $e$ is the void ratio, $b$ is a parameter describing void ratio effects on the water retention behaviour. Compared to van Genuchten's (1980) model, there is only one more parameter (i.e., $b$) in Eq. (12). The new parameter can be calculated from an existing parameter (i.e., $\lambda$), as shown in Eq. (13b). Such a relationship between $b$ and $\lambda$ can ensure that the gravimetric water content of unsaturated soil is almost independent of porosity when suction is relatively high, consistent with many

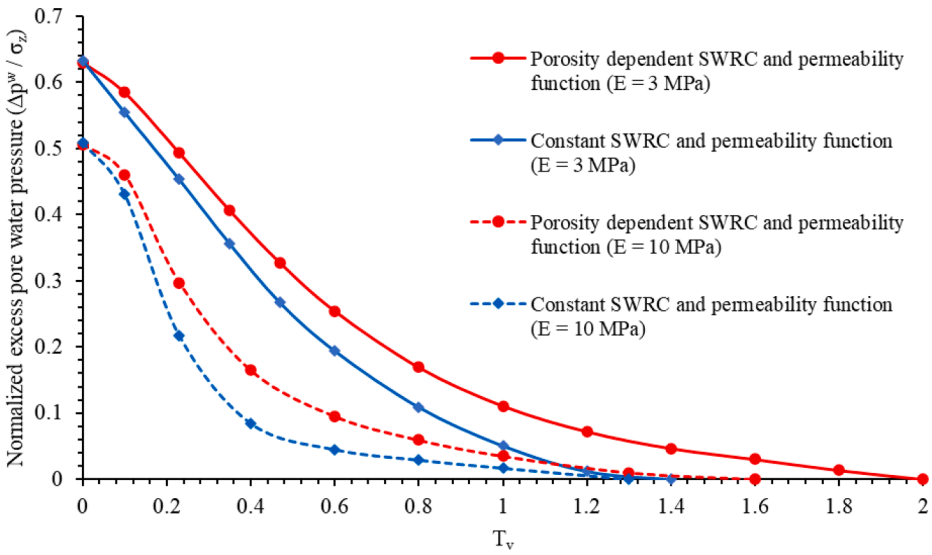


**Fig. 7.** Comparison between the computed consolidation behaviour with and without considering porosity effects on the hydraulic behaviour of unsaturated soil.

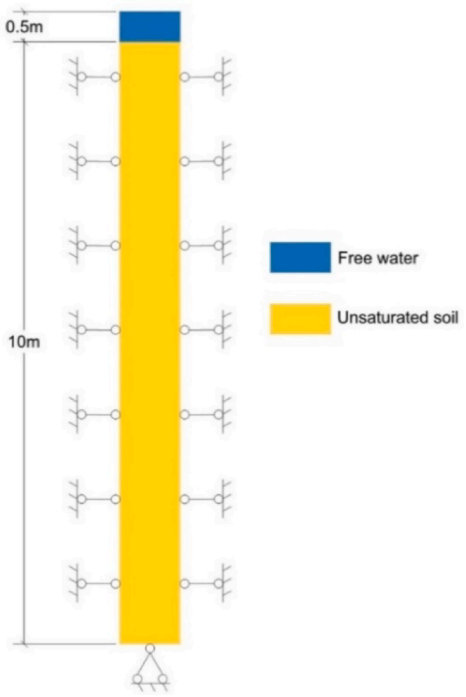


**Fig. 8.** Simulation of free water infiltration into an unsaturated soil column: geometry and boundary conditions.

experimental results (Tarantino, 2009). Apart from Tarantino (2009), some other researchers have proposed SWRC models with consideration of porosity effects (Gallipoli et al., 2003; Pasha et al., 2017; Pasha et al., 2020) and stress effects (Zhou & Ng, 2014). In particular, the model of Pasha et al. (2020) uses a constant effective stress parameter to simulate the influence of porosity on the SWRC of all soils, so no additional parameter is needed. It should be noted that the current study mainly focuses on rainfall-induced landslides, so only the wetting SWRC is modelled for simplicity. Ghaffaripour et al. (2019) illustrated that hysteresis effects should be considered if the problem involves a complex wetting–drying history.

On the other hand, the water permeability $k$ of unsaturated soil is modelled by the following equation:

$$k = k_{sat} k_r \tag{14}$$

where $k_{sat}$ is the saturated permeability, $k_r$ is the relative permeability for describing the influence of unsaturation on water permeability. The method of Mualem (1976) is used to determine the relationship between $k_r$ and the effective degree of saturation:

$$k_r = \sqrt{S_{eff}} \left[ 1 - \left( 1 - S_r^{\frac{1}{\lambda}} \right)^{\lambda} \right]^2 \tag{15}$$

In addition, $k_{sat}$ varies with porosity (Carrier, 2003):

$$k_{sat} = C \frac{n^3}{(1-n)^2} \tag{16}$$

where $C$ is a soil parameter. Eqs. (12) and (16) suggest that the SWRC, and saturated permeability are affected by porosity.

## 3. Numerical implementation

### 3.1. Space discretisation

As shown in Figs. 1 and 3, a continuum ($\Omega^l$ and $\Omega^s$) needs to be discretised into subdomains. The generalised interpolation material point method (GIMP) (Bardenhagen & Kober, 2004) is applied in this study. As it is shown in Fig. 4 (a), standard MPM uses an unsmooth linear shape function $N_I(x)$ for spatial discretisation, so the gradient of $N_I(x)$ ($\nabla N_I(x)$) is a piecewise function with a discontinuity at the corresponding central node $i$. When one material point in the element $e$ enters element $e+1$ by crossing node $i$, there are oscillations by using $\nabla N_I(x)$ for internal force calculation. GIMP uses a characteristic function $\chi_p(x)$ to define particles which is non-zero over a specific interval and zero elsewhere. A weight function $S_{Ip}$ and its gradient $\nabla S_{Ip}$ are used for spatial discretisation:

$$S_{Ip} = \frac{1}{V_p} \int_{\Omega_p} \chi_p(x) N_I(x) d\Omega \tag{17a}$$

$$\nabla S_{Ip} = \frac{1}{V_p} \int_{\Omega_p} \chi_p(x) \nabla N_I(x) d\Omega \tag{17b}$$

where $V_p$ is the volume of material points, $\Omega_p$ is the interval of characteristic function (see Fig. 4 (b)).

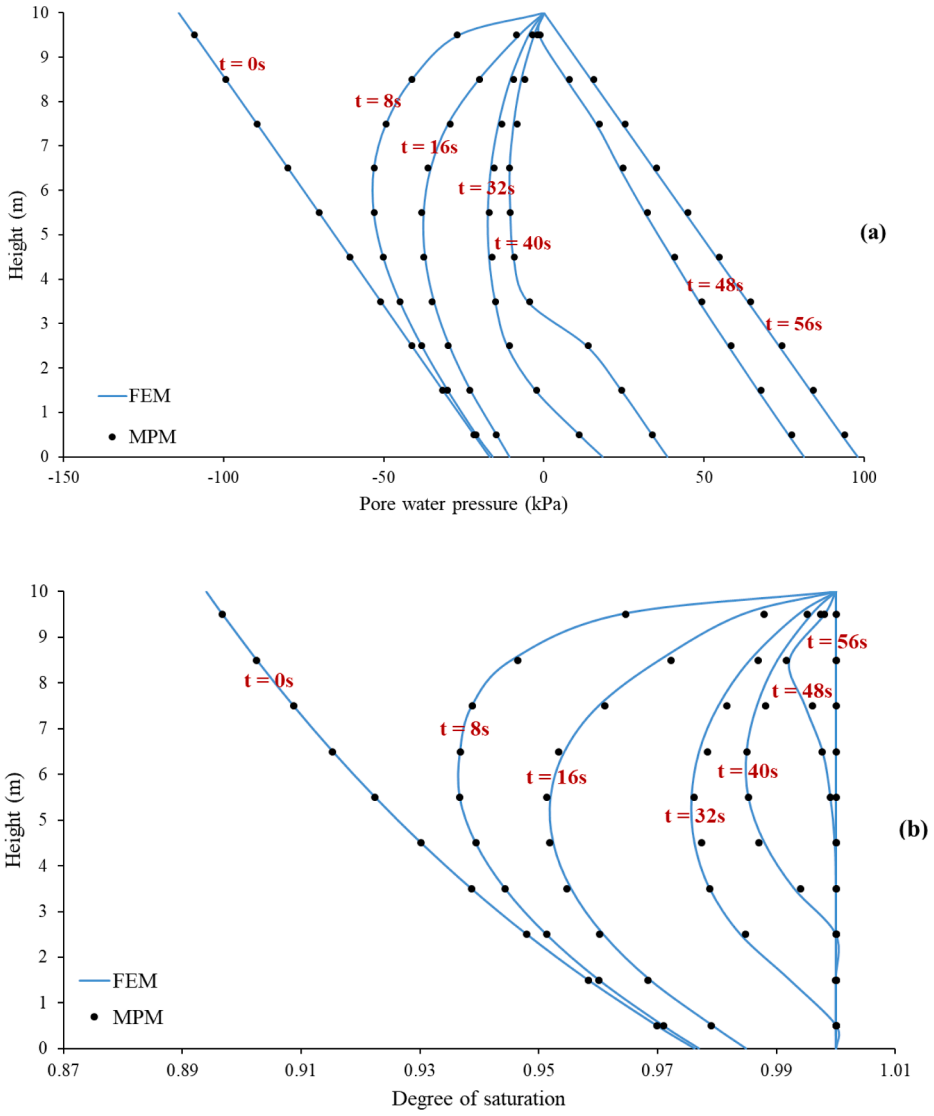


**Fig. 9.** Comparisons between FEM and MPM results of 1D infiltration tests: (a) pore water pressure distribution; and (b) degree of saturation distribution.

When $\sum_P \chi_p(x) = 1$, the weight function $S_{lp}$ is smooth and $\nabla S_{lp}$ is continuous. In general, an arbitrary MP property $f_p$ can be approximated at any point by the characteristic functions:

$$f(x) = \sum_p f_p \chi_p(x) \tag{18}$$

where $f(x)$ is an arbitrary continuous.

By setting the characteristic function equal to a Dirac delta function $\chi_p(x) = \delta(x - x_p)V_p$, the standard MPM can be derived from GIMP.

### 3.2. Discretisation of momentum balance equations

For the liquid phase, the momentum balance equation should be transformed into a weak form. Eq. (1) is multiplied by a test function $\boldsymbol{w}(x)$, which is the virtual velocity vector, and then integrated over the liquid phase domain $\Omega^l$:

$$\begin{aligned}\int_{\Omega^l} \rho^l(x)\dot{\boldsymbol{v}}^l(x)\boldsymbol{w}(x)d\Omega^l &= \int_{\Omega^w} \rho^l(x)\boldsymbol{g}(x)\boldsymbol{w}(x)d\Omega^l - \int_{\Omega^l} \nabla p^l(x)\boldsymbol{w}(x)d\Omega^l \\ &- \int_{\Omega^l} \frac{n(x)S_r(x)\rho^l(x)g}{k(x)}\left[\boldsymbol{v}^l(x) - \boldsymbol{v}^s(x)\right]\boldsymbol{w}(x)d\Omega^l\end{aligned} \tag{19}$$

Because the gradient of porosity is not considered, the final discrete form of Eq. (19) is given in Eq. (20):

$$\begin{aligned}\dot{\boldsymbol{v}}_I^l \sum_{lp} m_{lp}^l S_{Ilp} = &-\sum_{wp} \frac{n_{lp} m_{lp}^l g}{k_{lp}} \left(\boldsymbol{v}_{lp}^l - \boldsymbol{v}_{lp}^l\right) S_{Ip} - \int_{\partial\Omega^l} t^l(x) N_I(x) dS \\ &+ \sum_{lp} n_{lp} p_{lp}^l V_{lp} \nabla S_{Ilp} + \sum_{lp} m_p^l \boldsymbol{g}_{lp} S_{lp}^l\end{aligned} \tag{20}$$

where $m_{lp}^l$ is the equivalent mass of liquid point, and $t^l(x)$ is the liquid pressure boundary condition.

Similarly, for the solid–fluid mixture, the weak form of Eq. (4) is given by Eq. (21):

$$\begin{aligned}&\int_\Omega [1 - n(x)]\rho^s(x)\dot{\boldsymbol{v}}^s(x)\boldsymbol{w}(x)dV + \int_\Omega n(x)S_r(x)\rho^l(x)\dot{\boldsymbol{v}}^l(x)\boldsymbol{w}(x)dV \\ &= \int_\Omega div(\boldsymbol{\sigma})\boldsymbol{w}(x)dV + \int_\Omega [1 - n(x)]\rho^s(x)\boldsymbol{g}(x)\boldsymbol{w}(x)dV \\ &+ \int_\Omega n(x)S_r(x)\rho^l(x)\boldsymbol{g}(x)\boldsymbol{w}(x)dV\end{aligned} \tag{21}$$

In addition, the discretised form of Eq. (21) is as follows:

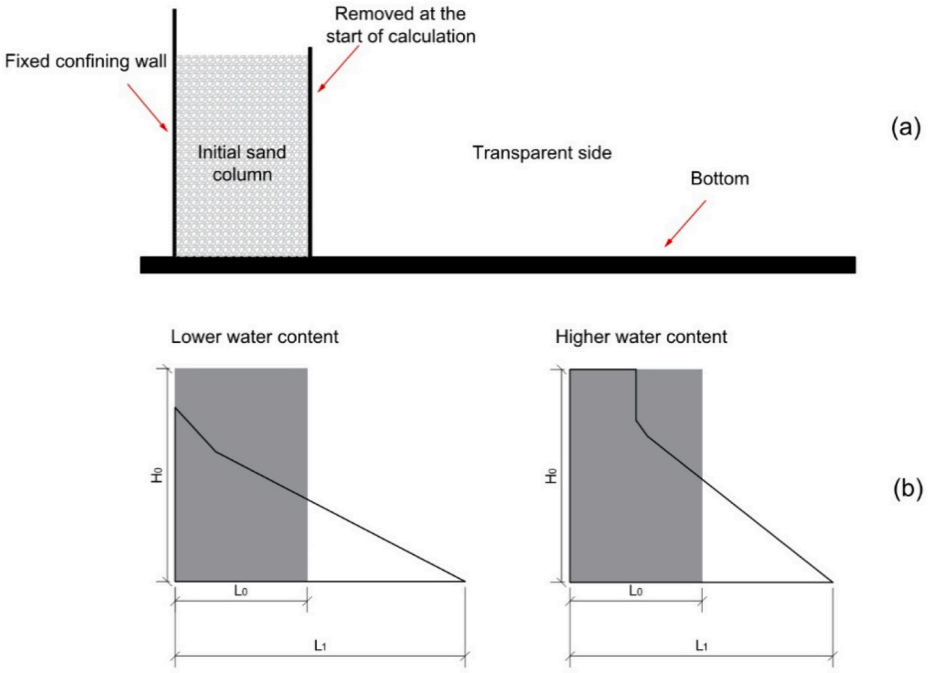


**Fig. 10.** Simulation of sand column collapse: (a) sketch of the sand column collapse test and (b) definition of the run-out length of sand column (after Santomaso et al., 2018).

**Table 2**
Material characteristics for sand column collapse.

| | |
|---|---|
| Water bulk modulus, $K^l$ | 2.2 GPa |
| Solid density, $\rho^s$ | 2800 kg/m$^3$ |
| Water density, $\rho^l$ | 1000 kg/m$^3$ |
| Solid Young's modulus, E | 50 MPa |
| Poisson's ratio, $\nu$ | 0.33 |
| Porosity, n | 0.4 |
| Saturated permeability, $k_{sat}$ | 4.41 × 10$^{-6}$ m/s |
| $S_{res}$ | 0 |
| a | 18.4 |
| λ | 0.63 |
| Cohesion, c | 0 |
| Friction angle, φ | 35° |
| Dilation angle, ψ | 0° |
| Tensile strength, $\sigma_t$ | 0 |

$$\dot{\boldsymbol{v}}_I^s \sum_{sp} m_{sp}^s S_{Isp} + \dot{\boldsymbol{v}}_I^l \sum_{lp} m_{lp}^l S_{Ilp} = \int_{\partial\Omega^s} \boldsymbol{t}(x)\boldsymbol{w}(x)dA - \sum_{sp} \boldsymbol{\sigma}_{sp}^* V_{sp} \nabla S_{Isp} + \sum_{lp} S_{rlp} p_{lp}^l V_{lp} \nabla S_{Ilp} + \boldsymbol{g}_I \sum_{sp} m_{sp}^s S_{Isp} + \boldsymbol{g}_I \sum_{lp} m_{lp}^l S_{Ilp} \quad (22)$$

where $\boldsymbol{t}(x)$ is the stress boundary condition.

### 3.3. Time discretisation

For time discretisation, $\Delta t$ is the time step:

$$t_{k+1} = t_k + \Delta t \quad (23)$$

Regarding the multi-phase MPM formulations for unsaturated soil, multiple criteria for the critical time step should be considered to achieve a stable solution (Yerro et al., 2022). The current study adopts two criteria for the solid and liquid phases. The first one is a permeability-dependent criterion (Mieremet et al., 2016) related to the dissipation of excess pore pressure. The other one is the Courant-Friedrichs-Levy criterion (Courant et al., 1967) related to compression wave propagation within the solid–fluid mixture. The critical time step takes the smaller value obtained from these two criteria.

The forward Euler scheme is used to update the velocity and displacement of the grid node.

$$\boldsymbol{v}_{k+1}^{\alpha} = \boldsymbol{v}_k^{\alpha} + \Delta t \dot{\boldsymbol{v}}_k^{\alpha} \quad (24)$$

$$\boldsymbol{u}_{k+1}^{\alpha} = \boldsymbol{u}_k^{\alpha} + \Delta t \boldsymbol{v}_k^{\alpha} \quad (25)$$

The Jacobian of deformation $J_k$ is used to obtain the volume change between the initial configuration $\Omega_0^s$ and the configuration at the $k^{th}$ time step $\Omega_k^s$ for the solid phase:

$$J_k = \frac{\Omega_k^s}{\Omega_0^s} = \frac{(1-n_k)\rho^s}{(1-n_0)\rho^s} \quad (26)$$

where $n_0$ is the initial porosity, and $n_k$ is porosity at time step $k$. According to Eq. (26), $n_k$ is updated by Eq. (27),

$$n_k = 1 - \frac{1-n_0}{J_k} \quad (27)$$

### 3.4. Computational procedures

Fig. 3 shows the MPM algorithm for each time increment, and the detailed computational procedures are summarised below:

(a) Map the information of material points to background nodes using the shape functions, including masses of the solid and liquid phases, the momentum of the solid and liquid phases, porosity stored in the solid material points and degree of saturation stored in the liquid material points;
(b) Interpolate the porosity to the liquid material points;
(c) Interpolate the degree of saturation to the solid material points;
(d) Calculate the acceleration of the liquid phase on the background nodes using Eq. (20);
(e) Calculate the acceleration of the solid phase on the background nodes using Eq. (22);

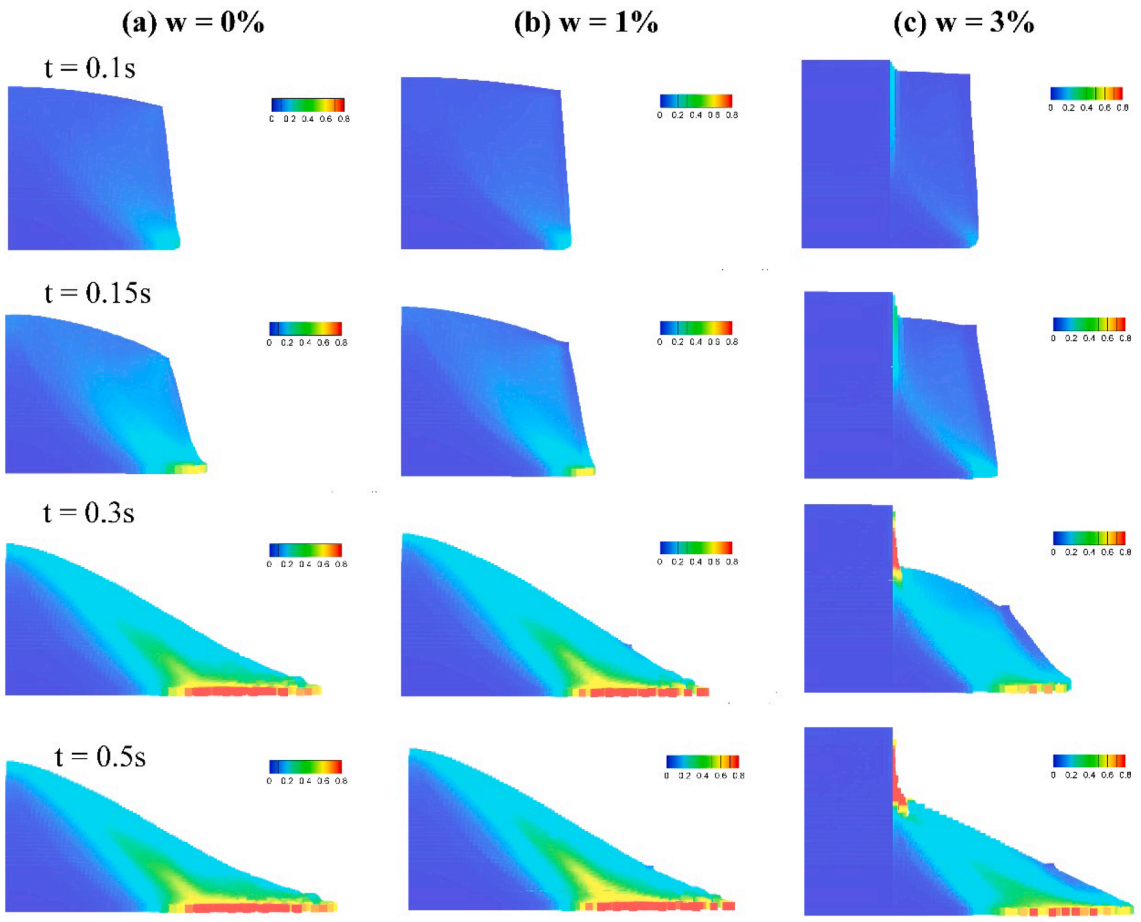


**Fig. 11.** Plastic strain contour at four different times (0.1, 0.15, 0.3 and 0.5s) calculated using MPM for (a) w = 0 % ($S_r = 0$) (b) w = 1 % ($S_r = 0.042$); (c) w = 3 % ($S_r = 0.126$).

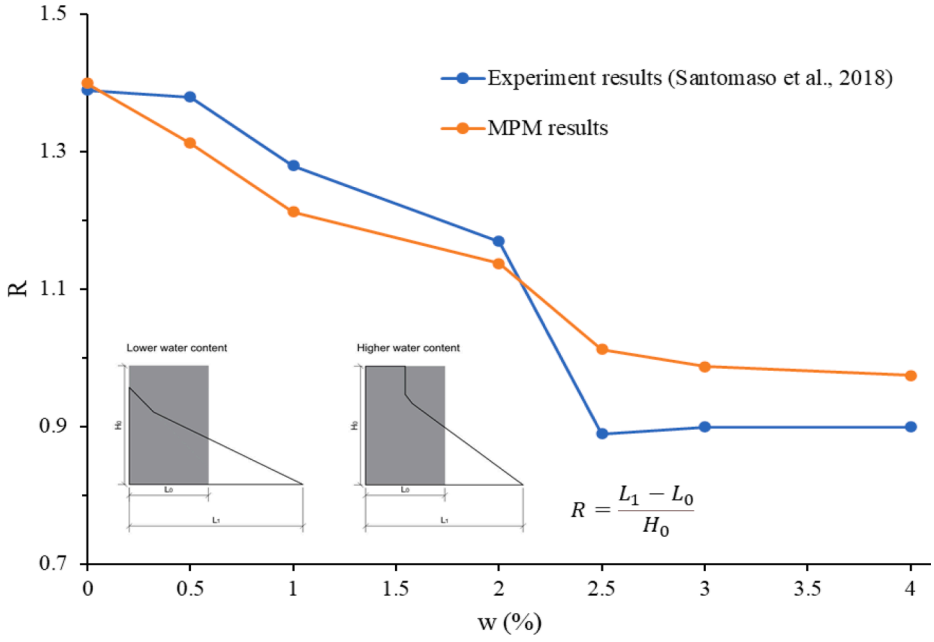


**Fig. 12.** Comparisons between experimental and MPM results of sand column tests with different water contents.

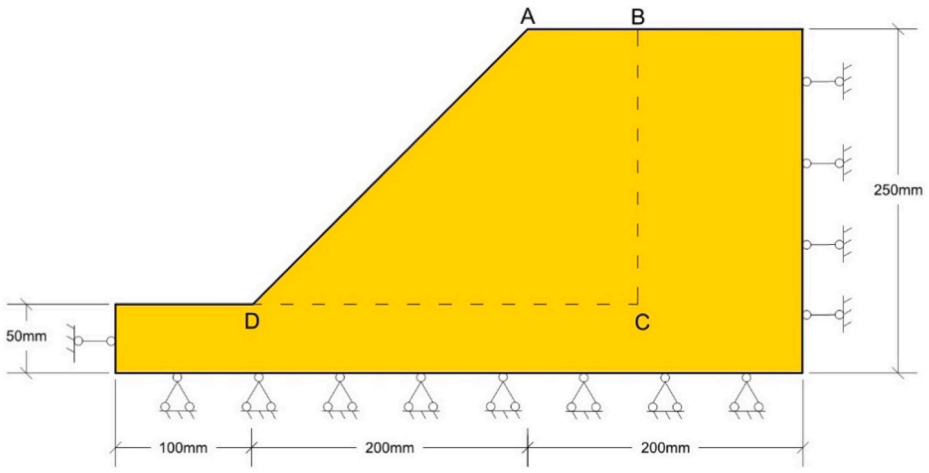


**Fig. 13.** Back-analysis of a centrifuge model test on an unsaturated sand slope subjected to rainfall (the displacement in Zone ABCD was measured during the test).

**Table 3**
Material characteristics for centrifuge model test.

| | |
|---|---|
| Water bulk modulus, $K^l$ | 2.2 GPa |
| Solid density, $\rho^s$ | 2670 kg/m$^3$ |
| Water density, $\rho^l$ | 1000 kg/m$^3$ |
| Solid Young's modulus, E | 10 MPa |
| Poisson's ratio, $\nu$ | 0.33 |
| Porosity, n | 0.48 |
| $S_{res}$ | 0 |
| Saturated permeability, $k_{sat}$ | $2.77 \times 10^{-3}$ m/s |
| a | 1.2 |
| $\lambda$ | 0.89 |
| Cohesion, c | 0 |
| Friction angle, $\varphi$ | 31.8° |
| Dilation angle, $\psi$ | −5° |
| Tensile strength, $\sigma_t$ | 0 |

(f) Update the velocities and positions of solid and liquid material points using Eqs. (24) and (25);
(g) Update the water pressure using Eqs. (9), as well as the degree of saturation and relative permeability byEqs. (12) and (15);
(h) Calculate the strain increment and update the Bishop's stress by Eq. (11) and porosity by Eq. (27);
(i) Initiate the background grid for the next step and store all the updated information in material points.

It should be noted that as a mesh-free numerical method, the MPM combines the Lagrangian and Eulerian descriptions. During the deformation process, the Lagrangian description is applied for the material points, while the Eulerian description is used for the stationary mesh generated in each time step.

## 4. Verification of the MPM formulation

To validate the new MPM formulation, it was applied to simulate five different problems: (i) Consolidation of saturated and unsaturated soils; (ii) Infiltration of the ponded water into unsaturated soil; (iii) Sand column collapse with various moisture conditions; (iv) Rainfall-induced failure of an unsaturated sand slope; (v) Transient seepage and instability of an unsaturated clay slope subjected to rainfall. Results from (i), (ii) and (v) are compared to those obtained using the FEM software Plaxis 2D. Details of this software were reported by Brinkgreve et al. (2016). Constitutive models in the FEM analysis are introduced in the following sections.

In both MPM and FEM simulations, a relatively high saturated water permeability was used to reduce computational time. Results from (iii) and (iv) are compared to the results of physical model tests (Santomaso et al., 2018; Wang et al., 2021). These five problems can be used to evaluate different aspects of the MPM formulation.

In the MPM simulations (iii), (iv) and (v), a small value of damping ($\alpha = 0.05$) is adopted to simulate the fraction between soil grains. The calculation stability could also be increased because of the friction-induced energy loss.

### 4.1. Consolidation of saturated and unsaturated soils

The consolidation of saturated and unsaturated soils is simulated using the numerical model shown in Fig. 5. The soil column's total height equals 1m. The size of each cell is 0.1m × 0.1m × 0.1m, and there are 8 points for each of the solid and liquid phases in one cell. An isotropic and homogeneous sandy clay is considered. The input parameters and their values are summarised in Table 1. Regarding boundary conditions, the top surface is permeable and free to move. A total vertical stress of 10 kPa is applied. The lateral boundaries are impermeable and fixed for horizontal displacement. The bottom of the soil column is impermeable, and no displacement is allowed in all directions. Two different initial conditions are considered: fully saturated condition with $S_r = 1$ and unsaturated condition with $S_r = 0.86$. The results of these two cases can be compared to reveal the influence of unsaturation on consolidation.

Fig. 6 shows the numerical results for both MPM and FEM simulations. The spatial and temporal variations of normalised excess pore water pressure are given. The normalised excess pore water pressure is a dimensionless parameter defined as the ratio of excess pore water pressure to the total vertical stress $\sigma_z$ applied at the top boundary. In addition, a dimensionless time $T_v$ is also used:

$$C_v = \frac{k}{m_v \rho^w g} \tag{28}$$

$$T_v = \frac{C_v}{H^2} t \tag{29}$$

where $C_v$ is the coefficient of consolidation, $m_v$ is the coefficient of volume compressibility, and $H$ is the soil layer thickness.

Upon the application of total stress to the soil, excess pore water pressure is generated in the beginning ($T_v = 0$). Under the saturated condition, the excess pore water pressure is equal to $\sigma_z$ and the total stress is carried by soil water only. In contrast, it is only equal to $0.51\sigma_z$ under unsaturated conditions because the compressibility of pore air is high, and part of the total stress is transferred to the soil skeleton. With an increase in $T_v$, water flows out of the soil skeleton from the top boundary, and excess pore water pressure dissipates. Finally, the normalised excess pore water pressure reduces to 0. The MPM and FEM

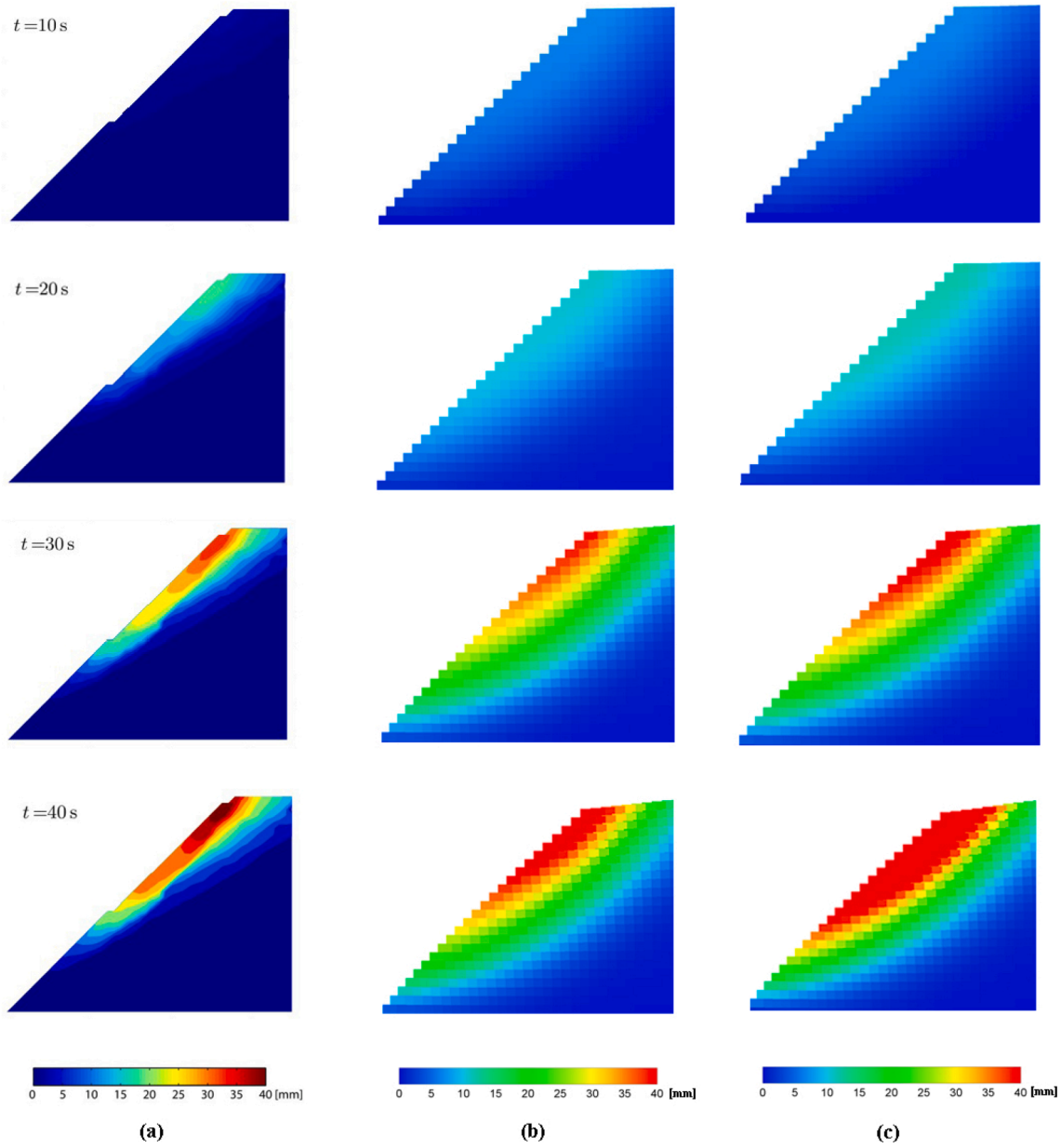


**Fig. 14.** Pre-failure soil displacement in Zone ABCD when the unsaturated sand slope is subjected to rainfall (a) measured in the centrifuge test (Wang et al., 2021); (b) MPM results considering porosity effects on SWRCC and permeability function; and (c) MPM results with constant SWRC and permeability function.

analysis results are well-matched for both saturated and unsaturated conditions.

The influence of porosity change on the water retention curve and permeability function is incorporated in this study. To evaluate the significance of this modification, unsaturated soil consolidation is simulated using two different methods. One incorporates the change of soil porosity in Eqs. (12) and (16), whereas the other case determines the water retention curve and permeability function using the initial porosity. In each case, two Young's moduli of 3 and 10 MPa are considered. Fig. 7 shows the normalised excess pore water pressure (i.e., the ratio of excess pore water and increment of total stress) in these two cases. The relationship between excess pore water pressure and time is similar at different locations, and results at the height of 0.25 cm are presented here as one example. At zero time ($T_v = 0$), the normalised excess pore water pressures in these two cases are close. During the process of consolidation with increasing $T_v$, water flows out of the soil skeleton, and the excess pore water pressure reduces. By incorporating the porosity dependency of hydraulic behaviour, the consolidation time increases from about $T_v = 1.4$ to $T_v = 2$ when Young's modulus is 3 MPa, consistent with the finding of Ghaffaripour et al. (2019) based on FEM analysis. The increase in consolidation time is mainly attributed to a lower permeability when the consolidation-induced porosity reduction is considered in Eq. (16). When Young's modulus increases to 10 MPa, the difference between these two cases becomes smaller because the porosity change is lower.

### 4.2. Ponded free water infiltration into unsaturated soil

The infiltration of ponded free water into a soil column is simulated using the numerical model in Fig. 8. Such a simulation requires the code to consider both free water outside the soil and pore water inside the soil, which can be readily achieved by using the two-point MPM approach but not the one-point MPM method. The total height of the soil layer equals 10m. The mesh size is 1m × 1m × 1m, and there are 8 points for each phase in one cell. The soil type is the same as that in Section 5.1. A linear elastic model is also applied for the soil skeleton. Above the soil,

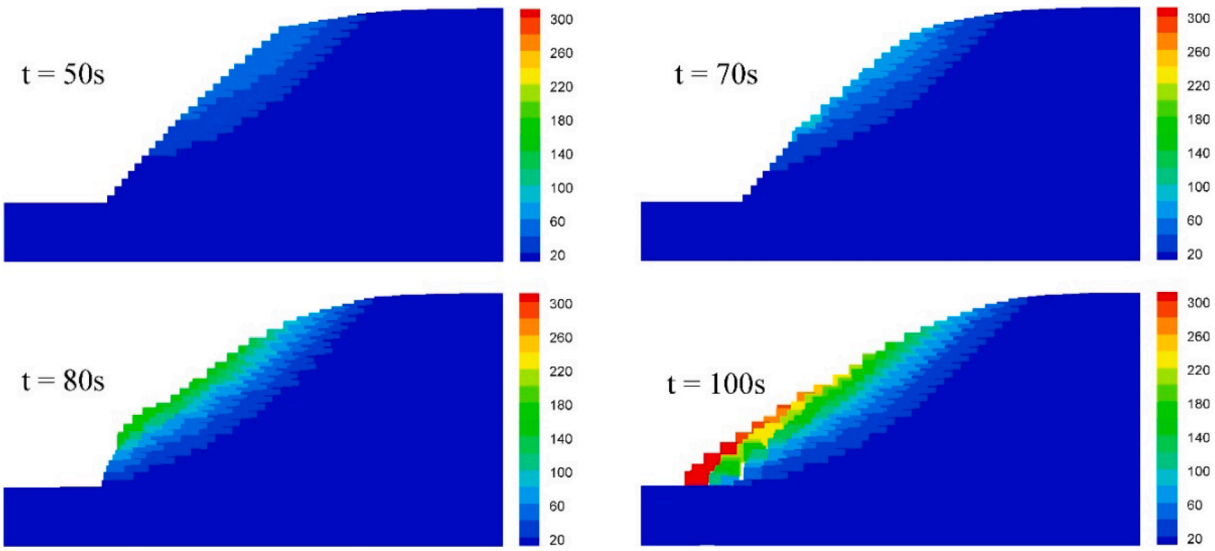


**Fig. 15.** Post-failure soil displacement (unit: mm) at four different times calculated using MPM.

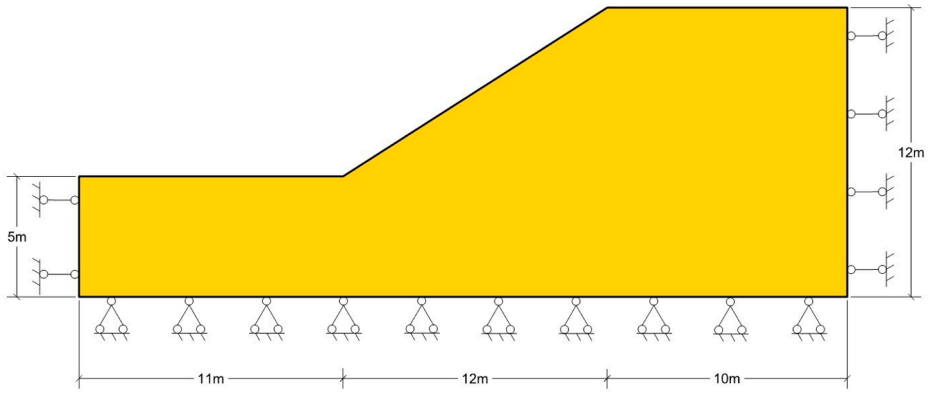


**Fig. 16.** Simulation of water seepage and slope instability under rainfall: geometry and boundary conditions.

**Table 4**
Material characteristics for rainfall-induced unsaturated landslide.

| | |
|---|---|
| Water bulk modulus, $K^l$ | 2.2 GPa |
| Solid density, $\rho^s$ | 2800 kg/m$^3$ |
| Water density, $\rho^l$ | 1000 kg/m$^3$ |
| Solid Young's modulus, E | 10 MPa |
| Poisson's ratio, $\nu$ | 0.33 |
| Porosity, n | 0.4 |
| Saturated permeability, $k_{sat}$ | 5 m/s |
| $S_{res}$ | 0.26 |
| a | 15.2 |
| $\lambda$ | 0.19 |
| Cohesion, c | 0 |
| Friction angle, $\varphi$ | 20° |
| Dilation angle, $\psi$ | 0° |
| Tensile strength, $\sigma_t$ | 0 |

the layer is ponded water with a thickness of 0.5 m. Within this range, there are only liquid material points. The two sides of the column are impermeable and fixed for horizontal displacement, and the bottom boundary is impermeable, and no displacement is allowed in all directions.

Fig. 9 shows the computed results by the MPM and FEM. In the MPM analysis, free water at the ground surface is modelled using liquid material points with an initial thickness of 0.5 m. The interface between the free water and soil column is assumed to be impermeable before the simulation of water infiltration. The initial pore water pressure inside the soil column is hydrostatic, increasing from −114 kPa at the top to −17 kPa at the bottom. At zero time, the interface is changed to a permeable boundary to simulate the water infiltration process. It is noted that the pore water at the soil top surface changes to a value close to zero rather than 5 kPa (equivalent to the hydrostatic pressure by a 0.5 m thick layer of water), mainly because the infiltration process is transient. On the other hand, the FEM analysis has a slightly different boundary condition from the MPM simulation because the FEM software Plaxis cannot model free water. The FEM analysis uses zero pore water pressure at the soil surface, which is very close to that obtained in the MPM analysis. The minor difference in boundary conditions would not influence the infiltration process too much. Upon the infiltration and downward flow of water, the pore water pressure and degree of saturation of soil increase with time. Under equilibrium conditions, all soils in the column become fully saturated. The pore water pressure follows the hydrostatic distribution, and the degree of saturation is 1. For the comparisons between MPM with FEM results, they are quite consistent. Taking the degree of saturation as an example, the maximum difference is about 1 %.

### 4.3. *Sand column collapse tests with different initial water contents*

Santomaso et al. (2018) conducted a series of sand column collapse tests considering soil moisture effects. As shown in Fig. 10 (a), the sand particles are initially put in a rectangular box, and the particle diameters

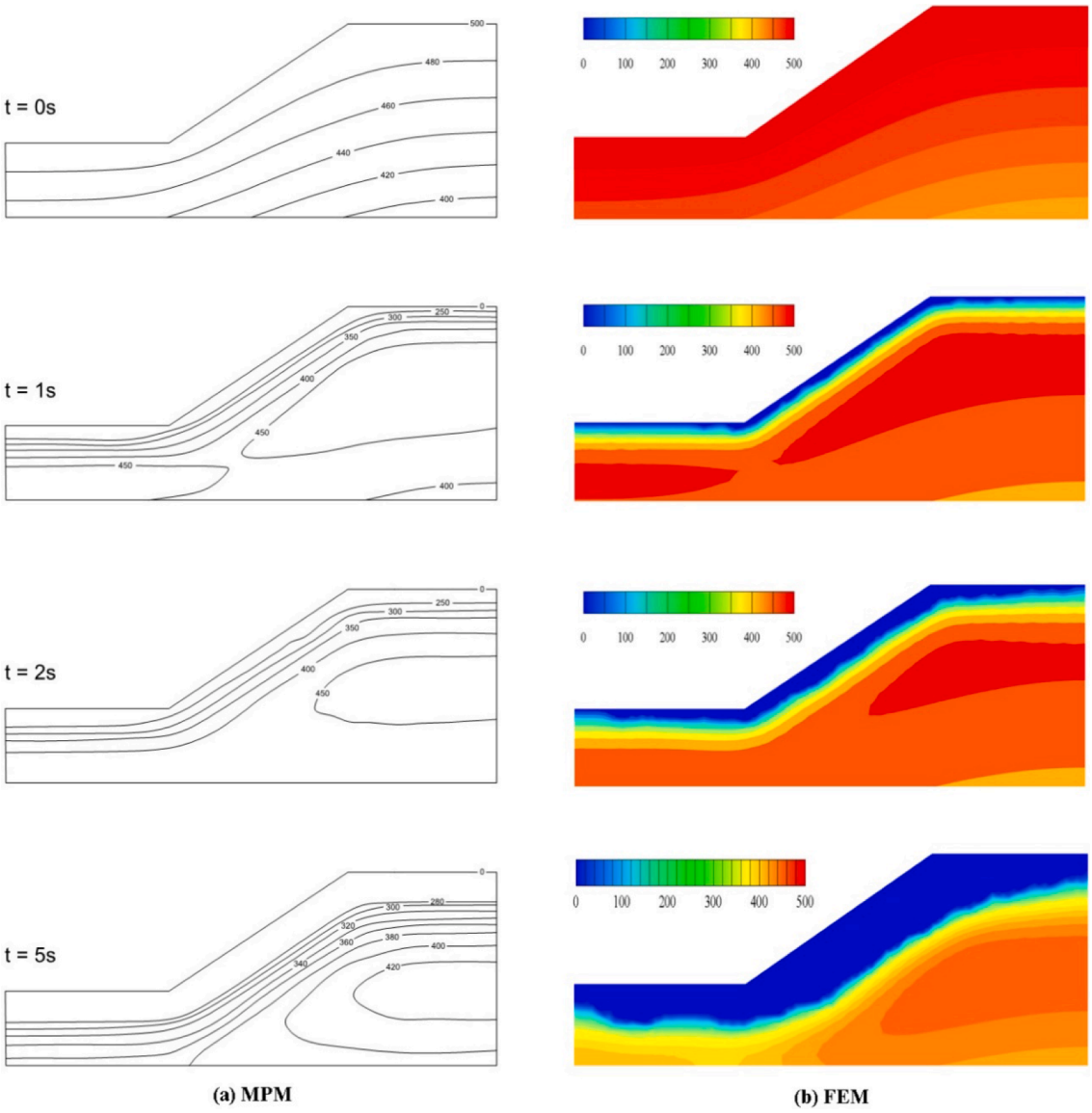


**Fig. 17.** Suction contour (unit: kPa) at four different times (0, 1, 2 and 5s) calculated using (a) MPM; and (b) FEM.

range from 2 to 2.2 mm. They considered different initial water contents, ranging from 0% to 4%. Then, the plate at the right boundary is removed to induce the collapse of the sand column. Fig. 10 (b) shows the typical profiles before and after the collapse. $H_0$ and $L_0$ are the initial height and length of the sand column, respectively. In this study, the initial sand column size is $0.007 \times 0.008$ m. $L_1$ is the final length related to the run-out distance.

The experimental results are used to verify the proposed MPM code. The boundary condition, initial condition and procedures in the numerical simulation are the same as those in the physical model tests. Details of the input parameters are given in Table 2. For the shear strength parameters of the sand, the friction angle and cohesion are determined based on ring shear tests by Santomaso et al. (2018) with the assumption of zero dilation angle and zero cohesion. The parameters for water retention behaviour ($S_{res}$, $a$ and $\lambda$) are estimated using the semi-empirical equations of Carsel and Parrish (1988), which correlates these parameters with the porosity and particle size distribution of soil. Other parameters, including the saturated permeability, Young's modulus and Poisson's ratio, use the typical value of sand based on the study of Liu et al. (2017) and Feng et al. (2021).

Fig. 11 (a) shows the plastic strain contours and granular flow process at four different times with zero water content. It is clear that a large plastic strain first occurs in the sand column's toe. Then the slip surface is developed, and a wedge shape slip mass is formed. The soil mass above the failure surface moves along the slip surface and then flows along the bottom boundary. Fig. 11 (b) and (c) show the failure process at 1 % and 3 % water contents. With increased water content, sand column deformation becomes smaller at a given time. The slope of the slip surface becomes steeper, and the slipping mass above the failure surface becomes smaller. For a relatively higher water content ($w = 3\%$), a partial collapse behaviour is observed in Fig. 11 (c).

Fig. 12 shows the relationship between initial water content and the run-out distance. A dimensionless parameter $R = \frac{L_1 - L_0}{H_0}$ is applied to evaluate the sand mechanical behaviour, the definition of which can be traced back to a simple energy balance (Iverson, 1997). An increase in water content results in a smaller $R$ value, particularly when the water content is less than 2 %. The numerical model can well capture this trend

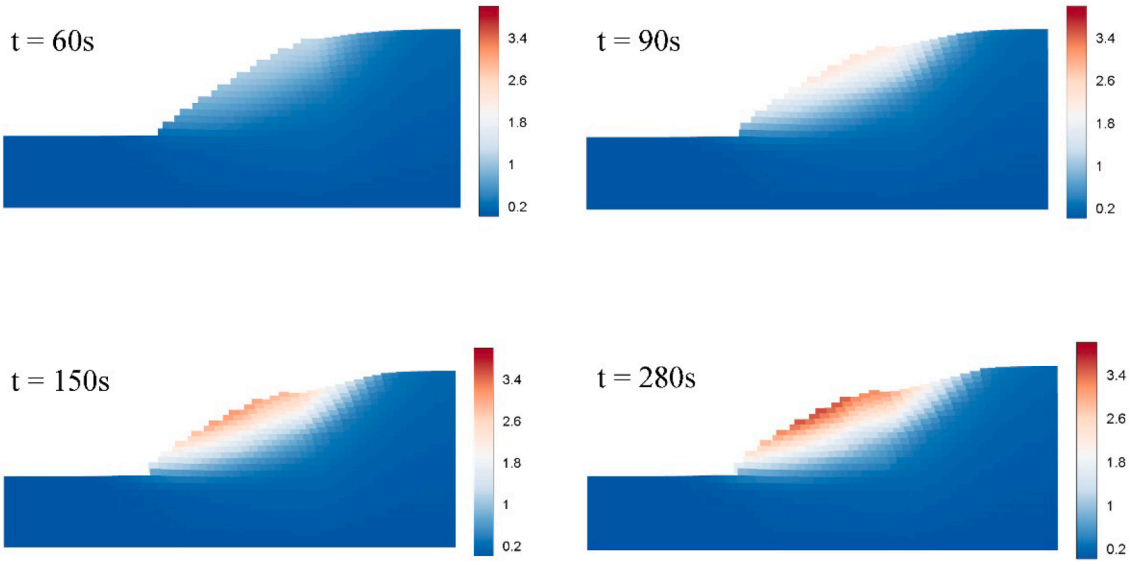


**Fig. 18.** Displacement contour (unit: m) at four different times (60, 90, 150 and 280s) calculated using MPM.

because the increase in water content (degree of saturation) reduces the Bishop's effective stress (see Eq. (11)). When water content ranges from 2.5 % and 4 %, the change in $R$ value is very small. After all, the value of Bishop's effective stress is almost content within this range. Based on the above analysis in Figs. 9 and 10, the triggering and motion of the granular flow process can be well captured by the proposed numerical method.

### 4.4. Rainfall-induced failure of an unsaturated sand slope

The proposed MPM formulation is used to simulate one centrifuge model test reported by Wang et al. (2021). Fig. 13 shows the geometry of soil slope in the MPM model, consistent with the test condition of Wang et al. (2021). The slope height equals 200mm, and the slope angle is 45°. The test and numerical simulations were finished at 30-g, so the slope height is 6 m at the prototype scale. The cell size equals 10mm × 10mm × 10mm, and there are eight material points for each phase in one cell. The soil is well-graded silty sand with a mean grain diameter $d_{50}$ of 0.23 mm. Details of the input parameters are shown in Table 3. The silty sand parameters are determined in an approach similar to Section 4.3, so the calibration method is briefly explained here. The triaxial tests of Wang et al. (2021) are used to calibrate the peak friction angle, cohesion and water retention parameters. According to the test results of Wang et al. (2021), there is a volumetric contraction for the silty sand at a loose state, so a negative dilation angle ($\psi^{peak} = -5^{\circ}$) to simulate strain-hardening with $\gamma^{peak} = 0.01$ and $\gamma^{crit} = 0.2$. In addition, Young's modulus and Poisson's ratio use the typical values of silty sand.

Regarding the boundary conditions, the ground surface is permeable and free to move. The heavy rainfall condition is simulated by maintaining zero suction at the ground surface after an equilibrium state is achieved at the prescribed g-level (initial water content $w_0 = 11.5\%$ and suction $s = 9.2$kPa). The lateral boundaries are impermeable and fixed for horizontal displacement. The bottom boundary is impermeable, and no displacement is allowed in any direction. Under rainfall, the slope failure occurs at 40s in the centrifuge model test and 50s in the numerical simulation.

As illustrated above, the porosity dependency of hydraulic properties (Eqs. (12) and (16)) can greatly affect the consolidation behaviour of unsaturated soil, particularly when Young's modulus is lower. To further investigate the role of these two equations, rainfall-induced landslides are simulated with and without considering the influence of porosity change on the SWRC and permeability function. The results are shown in Fig. 14 and compared with the experimental results measured using the GeoPIV at four different times: $t_1 = 10$s, $t_2 = 20$s, $t_3 = 30$s, $t_4 = 40$s. Large displacement mainly occurs at the upper part of the slope (i.e. Zone ABCD in Fig. 13), and the maximum displacement is located at the slope crest. When the porosity dependency of SWRC and permeability function is considered, the measured and computed results are more consistent, and the displacement is smaller. These two findings are because the test soil shows contractive behaviour (Wang et al., 2021) during the process of slope deformation. When the porosity effects on dependent SWRC are considered through Eq. (12), the soil is expected to have a higher water retention ability. Consequently, a higher equilibrium suction is predicted at a given degree of saturation, leading to lower relative permeability and higher strength. Moreover, there is a decrease in saturated permeability when porosity effects are included in Eq. (16), resulting in a smaller amount of rainfall infiltration and, therefore, a smaller slope displacement.

Fig. 15 shows the post-failure soil displacement. At $t = 50$s, the slope failure occurs, and the maximum displacement is about 40mm. From $t = 70$s to $t = 100$s, the top part of the slope continues moving down. The average depth of the sliding Zone is about 0.93m at the prototype scale. The shallow slope failure is caused by rainfall infiltration-induced suction loess, which reduces the value of Bishop's stress.

### 4.5. Rainfall-induced failure of an unsaturated clay slope

As illustrated in Section 4.4, the proposed MPM formulation can well simulate rainfall-induced landslide. This section further studies the failure process of an unsaturated clay slope subjected to rainfall. Fig. 16 shows the geometry of this slope. Similar to the study by Alonso et al. (2010), the slope height equals 7m, and the slope angle is about 32.5°. The cell size equals 0.5m × 0.5m × 0.5m, and there are eight material points for each phase in one cell. The soil is a medium-plasticity sandy clay based on the classification method of the United States Department of Agriculture (1966). Details of the input parameters are shown in Table 4. Shear strength parameters are from direct shear tests by Alonso et al. (2010). A constant value of friction angle is used with zero cohesion and dilation angle. The water retention parameters are obtained using the Carsel and Parrish (1988) method explained in Section 4.3. Typical values of the clay stiffness parameters are used. Compared with Table 3, there is a great difference in hydraulic properties between the silty sand and sandy clay, which significantly influences water infiltration and slope failure.

Initially, the slope is in equilibrium with the gravity force and the prescribed suction ($s = 500$kPa) along the ground surface. Regarding the boundary conditions, the ground surface is permeable and free to move. The rainfall is simulated by maintaining zero suction at the ground surface. The lateral boundaries are impermeable and fixed for horizontal displacement. The bottom boundary is impermeable, and no displacement is allowed in any direction.

Fig. 17 plots the suction contour computed using the MPM and FEM at four different times: $t_1 = 0$s, $t_2 = 1$s, $t_3 = 2$s, $t_4 = 5$s. The results at a longer time (above 5s) are not compared because soil deformation becomes too large; thus, the FEM does not give a convergent result. It is clear from Fig. 17 that the wetting front goes deeper during the rainfall process, and suction loss occurs. When $t = 5$s, the top 2m reaches a fully saturated condition. By comparing MPM and FEM results, at all times, they are well matched.

According to Eq. (11), the Bishop's stress decreases, resulting in a landslide. Fig. 18 shows the displacement contours from the MPM simulation to study the failure process. At $t = 60$s, a non-zero displacement zone appears. At $t = 90$s, a corresponding large value of slope displacement occurs. For a longer time, a clear failure surface is formed, the average depth of the slope surface is about 2m, and the slope surface is like a smooth arc.

## 5. Summary and Conclusions

In this study, a two-phase two-point MPM formulation is developed for the coupled hydro-mechanical behaviour of saturated and unsaturated soils. The proposed MPM formulation has newly incorporated the influence of porosity on the water retention ability and permeability function. Two distinct sets of material points represent the solid and liquid phases. Unlike the one-point method widely used in the previous MPM formulations for unsaturated soil, the two-phase two-point method can simulate both pore water and free water. The GIMP is used for spatial discretisation since it shows a better capability of minimising numerical oscillations than the standard MPM.

The rainfall-induced failure of unsaturated soil slope was simulated to evaluate the new code for analysing large deformation problems involving unsaturated soil. The computed results in the pre-failure stage are consistent with the centrifuge model test. Furthermore, a series of sand column collapse tests with different water contents were simulated. The measured and computed run-out distances at various moisture conditions are well-matched. The proposed MPM code can well simulate large displacement problems under unsaturated conditions.

Several geotechnical problems under small displacement were also studied, including the consolidation of saturated and unsaturated soils and the infiltration of ponded water into unsaturated soil. The results of MPM simulations were compared to those from the FEM simulations. Results obtained from these two methods are almost identical at the small-displacement stage, suggesting that the new code can give reliable results.

## CRediT authorship contribution statement

**Z.Q. Zhan:** Software, Data curation, Investigation, Writing – original draft. **C. Zhou:** Conceptualization, Methodology, Investigation, Supervision, Writing – original draft. **C.Q. Liu:** Methodology, Investigation, Writing – review & editing. **C.W.W. Ng:** Supervision, Writing – review & editing.

## Declaration of Competing Interest

The authors declare that they have no known competing financial interests or personal relationships that could have appeared to influence the work reported in this paper.

## Data availability

Data will be made available on request.

*Acknowledgements*

The authors would like to thank the Hong Kong Research Grants Council for providing financial support through grants AoE/E-603/18 and 15205721. Dr Chuanqi Liu is supported by the One Hundred Talents Program of the Chinese Academy of Sciences and National Natural Science Foundation of China (No. 12172368).

*Availability of data and materials*

Data are available from the authors upon reasonable request.

## References

Abe, K., Soga, K., Bandara, S., 2014. Material point method for coupled hydro-mechanical problems. J. Geotech. Geoenviron. Eng. 140 (3), 04013033.
Alonso, E.E., Pinyol, N.M., Puzrin, A.M., 2010. Geomechanics of failures: advanced topics. Springer.
Bandara, S., Soga, K., 2015. Coupling of soil deformation and pore fluid flow using material point method. Comput. Geotech. 63, 199–214.
Bardenhagen, S.G., Kober, E.M., 2004. The generalised interpolation material point method. Comput. Model. Eng. Sci. 5 (6), 477–496.
Beuth, L., 2012. Formulation and application of a quasi-static material point method.
Brinkgreve, R., Kumarswamy, S., Swolfs, W., et al., 2016. PLAXIS 2016. PLAXIS, the Netherlands.
Carrier III, W.D., 2003. Goodbye, hazen; hello, kozeny-carman. J. Geotech. Geoenviron. Eng. 129 (11), 1054–1056.
Carsel, R.F., Parrish, R.S., 1988. Developing joint probability distributions of soil water retention characteristics. Water Resour. Res. 24 (5), 755–769.
Ceccato, F., Yerro, A., Martinelli, M., 2018. Modelling soil-water interaction with the material point method. Evaluation of single-point and double-point formulations. In: Numerical methods in geotechnical engineering IX. CRC Press, pp. 351–358.
Ceccato, F., Yerro, A., Girardi, V., et al., 2021. Two-phase dynamic MPM formulation for unsaturated soil. Comput. Geotech. 129, 103876.
Chiu, C.F., Ng, C.W.W., 2003. A state-dependent elasto-plastic model for saturated and unsaturated soils. Géotechnique 53 (9), 809–829.
Courant, R., Friedrichs, K., Lewy, H., 1967. On the partial difference equations of mathematical physics. IBM J. Res. Dev. 11 (2), 215–234.
de Vaucorbeil, A., Nguyen, V.P., Sinaie, S., et al., 2020. Material point method after 25 years: Theory, implementation, and applications. Adv. Appl. Mech. 53, 185–398.
Feng, K., Huang, D., Wang, G., 2021. Two-layer material point method for modeling soil–water interaction in unsaturated soils and rainfall-induced slope failure. Acta Geotech. 16 (8), 2529–2551.
Fern, E., 2016. Constitutive modelling of unsaturated sand and its application to large deformation modelling. University of Cambridge. Ph. D. thesis,.
Fern, E.J., de Lange, D.A., Zwanenburg, C., et al., 2017. Experimental and numerical investigations of dyke failures involving soft materials. Eng. Geol. 219, 130–139.
Fern, J., Rohe, A., Soga, K., et al., 2019. The material point method for geotechnical engineering: a practical guide. CRC Press.
Gallipoli, D., Wheeler, S., Karstunen, M., 2003. Modelling the variation of degree of saturation in a deformable unsaturated soil. Géotechnique 53 (1), 105–112.
Ghaffaripour, O., Esgandani, G.A., Khoshghalb, A., et al., 2019. Fully coupled elastoplastic hydro-mechanical analysis of unsaturated porous media using a meshfree method. Int. J. Numer. Anal. Meth. Geomech. 43 (11), 1919–1955.
Higo, Y., Oka, F., Kimoto, S., et al., 2010. A coupled MPM-FDM analysis method for multi-phase elasto-plastic soils. Soils Found. 50 (4), 515–532.
Hu, Y., Randolph, M., 1998. A practical numerical approach for large deformation problems in soil. Int. J. Numer. Anal. Meth. Geomech. 22 (5), 327–350.
Iverson, R.M., 1997. The physics of debris flows. Rev. Geophys. 35 (3), 245–296.
Jassim, I., Stolle, D., Vermeer, P., 2013. Two-phase dynamic analysis by material point method. Int. J. Numer. Anal. Meth. Geomech. 37 (15), 2502–2522.
Khoshghalb, A., Khalili, N., 2015. An alternative approach for quasi-static large deformation analysis of saturated porous media using meshfree method. Int. J. Numer. Anal. Meth. Geomech. 39 (9), 913–936.
Lei, X., He, S., Chen, X., et al., 2020. A generalised interpolation material point method for modelling coupled seepage-erosion-deformation process within unsaturated soils. Adv. Water Resour. 141, 103578.
Liu, C., Sun, W., 2020. Shift boundary material point method: an image-to-simulation workflow for solids of complex geometries undergoing large deformation. *Computational Particle Mechanics* 7 (2), 291–308.
Liu, C., Sun, Q., Jin, F., et al., 2017. A fully coupled hydro-mechanical material point method for saturated dense granular materials. Powder Technol. 314, 110–120.
Lv, Y., Liu, H., Ng, C.W., Ding, X., Gunawan, A., 2014. Three-dimensional numerical analysis of the stress transfer mechanism of XCC piled raft foundation. Comput. Geotech. 55, 365–377.
Martinelli, M., Rohe, A., Soga, K., 2017. Modeling dike failure using the material point method. Procedia Eng. 175, 341–348.

Mieremet, M., Stolle, D., Ceccato, F., et al., 2016. Numerical stability for modelling of dynamic two-phase interaction. Int. J. Numer. Anal. Meth. Geomech. 40 (9), 1284–1294.
Mualem, Y., 1976. A new model for predicting the hydraulic conductivity of unsaturated porous media. Water Resour. Res. 12 (3), 513–522.
Ng, C.W.W., Zhou, C., Chiu, C.F., 2020. Constitutive modelling of state-dependent behaviour of unsaturated soils: an overview. Acta Geotech. 15 (10), 2705–2725.
Pasha, A.Y., Khoshghalb, A., Khalili, N., 2017. Hysteretic model for the evolution of water retention curve with void ratio. J. Eng. Mech. 143 (7), 04017030.
Pasha, A., Khoshghalb, A., Khalili, N., 2020. Evolution of isochoric water retention curve with void ratio. Comput. Geotech. 122, 103536.
Santomaso, A.C., Volpato, S., Gabrieli, F., 2018. Collapse and run-out of granular columns in pendular state. Phys. Fluids 30 (6), 063301.
Shafee, A., Khoshghalb, A., 2022. Particle node-based smoothed point interpolation method with stress regularisation for large deformation problems in geomechanics. Comput. Geotech. 141, 104494.
Soga, K., Alonso, E., Yerro, A., et al., 2016. Trends in large-deformation analysis of landslide mass movements with particular emphasis on the material point method. Géotechnique 66 (3), 248–273.
Song, D., Choi, C.E., Ng, C.W.W., Zhou, G.G.D., 2018. Geophysical flows impacting a flexible barrier: effects of solid-fluid interaction. Landslides 15 (1), 99–110.
Sulsky, D., Chen, Z., Schreyer, H.L., 1994. A particle method for history-dependent materials. Comput. Methods Appl. Mech. Eng. 118 (1–2), 179–196.
Tarantino, A., 2009. A water retention model for deformablesoils. Géotechnique 59 (9), 751–762.
Van Esch, J., Stolle, D., Jassim, I., 2011. Finite element method for coupled dynamic flow-deformation simulation. 2nd International Symposium on Computational Geomechanics.
Van Genuchten, M.T., 1980. A closed-form equation for predicting the hydraulic conductivity of unsaturated soils. Soil Sci. Soc. Am. J. 44 (5), 892–898.
Verruijt, A., 2009. An introduction to soil dynamics. Springer Science & Business Media.
Wang, D., Bienen, B., Nazem, M., et al., 2015. Large deformation finite element analyses in geotechnical engineering. Comput. Geotech. 65, 104–114.
Wang, S., Idinger, G., Wu, W., 2021. Centrifuge modelling of rainfall-induced slope failure in variably saturated soil. Acta Geotech. 16 (9), 2899–2916.
Wang, B., Vardon, P., Hicks, M., 2018. Rainfall-induced slope collapse with coupled material point method. Eng. Geol. 239, 1–12.
Więckowski, Z., 2004. The material point method in large strain engineering problems. Comput. Methods Appl. Mech. Eng. 193 (39–41), 4417–4438.
Yerro, A., Alonso, E., Pinyol, N., 2015. The material point method for unsaturated soils. Géotechnique 65 (3), 201–217.
Yerro, A., Alonso, E., Pinyol, N., 2016a. Run-out of landslides in brittle soils. Comput. Geotech. 80, 427–439.
Yerro, A., Pinyol, N.M., Alonso, E.E., 2016b. Internal progressive failure in deep-seated landslides. Rock Mech. Rock Eng. 49 (6), 2317–2332.
Yerro, A., Girardi, V., Martinelli, M., et al., 2022. Modelling unsaturated soils with the Material Point Method. A discussion of the state-of-the-art. Geomech. Energy Environ. 32, 100343.
Zabala, F., Alonso, E., 2011. Progressive failure of Aznalcóllar dam using the material point method. Géotechnique 61 (9), 795–808.
Zhang, X., Chen, Z., Liu, Y., 2016. The material point method: a continuum-based particle method for extreme loading cases. Academic Press.
Zhang, H., Wang, K., Chen, Z., 2009. Material point method for dynamic analysis of saturated porous media under external contact/impact of solid bodies. Comput. Methods Appl. Mech. Eng. 198 (17–20), 1456–1472.
Zhou, C., Ng, C.W.W., 2014. A new and simple stress-dependent water retention model for unsaturated soil. Comput. Geotech. 62, 216–222.
Zhou, C., Ng, C.W.W., 2016. Effects of temperature and suction on plastic deformation of unsaturated silt under cyclic loads. J. Mater. Civ. Eng. 28 (12), 04016170.
Zhou, C., So, P.S., Chen, X.W., 2020. A water retention model considering biopolymer-soil interactions. J. Hydrol. 586, 124874.
Zienkiewicz, O.C., Chan, A., Pastor, M., et al., 1990. Static and dynamic behaviour of soils: a rational approach to quantitative solutions. I. Fully saturated problems. Proc. Roy. Soc. London. A. Math. Phys. Sci. 429 (1877), 285–309.